



# Electron self-sufficient core-shell BiOCl@Fe-BiOCl nanosheets boosting Fe (III)/Fe(II) recycling and synergetic photocatalysis-Fenton for enhanced degradation of phenol

Zhaohui Wu<sup>a,b</sup>, Jie Shen<sup>a</sup>, Wenlu Li<sup>b</sup>, Junshan Li<sup>c</sup>, Donghao Xia<sup>a</sup>, Difa Xu<sup>a</sup>, Shiyong Zhang<sup>a,\*</sup>, Yongfa Zhu<sup>b,\*</sup>

<sup>a</sup> Hunan Key Laboratory of Applied Environmental Photocatalysis, Changsha University, Changsha 410022, Hunan Province, China

<sup>b</sup> Department of Chemistry, Tsinghua University, Beijing 100084, China

<sup>c</sup> Institute for Advanced Study, Chengdu University, Chengdu 610106, China

## ARTICLE INFO

### Keywords:

Electron self-sufficient  
Core-shell BiOCl@Fe-BiOCl  
Directional charge transfer  
Fe ions recycling  
Photocatalytic-Fenton performances

## ABSTRACT

Core-shell BiOCl@Fe-BiOCl nanosheets with electron self-sufficient structure were prepared as catalysts to promote degradation and mineralization of phenol through synergetic photocatalysis-Fenton. This electron self-sufficient structure was established by engaging a strong internal electric field of BiOCl core and electron-capture centers of doped Fe(III) in Fe-BiOCl shell for electrons supplying and consuming, respectively, separating charges spatially and enriching holes on the surface of catalysts. Meanwhile, the Fe(III) transitioned to Fe(II), which acted as reactive sites for H<sub>2</sub>O<sub>2</sub> activation and was further reversed to Fe(III) and hydroxyl radical (•OH) through Fenton reaction, achieving Fe(III)/Fe(II) recycling. The •OH and surface holes could synergistically boost the degradation and mineralization (~64 %) of phenol. The reaction rate constant of BiOCl@Fe-BiOCl nanosheets was ~41.32 and ~95 times higher than that of BiOCl under full spectra and visible light irradiation, respectively. This work provides sophisticated structure design of catalysts, boosting Fe(III)/Fe(II) recycling, catalytic activity, and mineralization.

## 1. Introduction

Phenolic contaminants in wastewater are a giant and sharply increasing threat to human health and the global environment, requiring efficient removal through economic and green technologies [1,2]. Photocatalytic oxidation of phenolic contaminants is considered as an appealing green technology. Because the phenolic pollutants could be mineralized into harmless in the presence of solar energy and photocatalysts [3–6]. Bismuth oxychloride (BiOCl) has been considered as a potential photocatalyst for containment removal due to its built-in internal electric field (IEF), stable structure, and appropriate band structure for strong oxidation ability [7–10]. However, the limited ultraviolet light response, inefficient charge separation, and sole active species of BiOCl have still restricted the photocatalytic oxidation efficiency of phenolic contaminants. Hence, many strategies have been exploited to modify band structure, and promote charge separation for boosted photocatalytic performances. Particularly, conducting homo-/heterostructure for enhanced interfacial IEF [11,12], elements doping or

vacancies introducing for band structure regulation [10,13,14], and constructing unique facets combination [15–17], were frequently used for spatial transfer and efficient separation of charge carriers, promoting the photocatalytic performances of BiOCl.

During the photocatalytic process, the reactive oxygen species including superoxide radical (•O<sub>2</sub><sup>-</sup>), peroxy radical (O<sub>2</sub><sup>-</sup>), hydroxyl radical (•OH), singlet oxygen (<sup>1</sup>O<sub>2</sub>) are the general species, especially •O<sub>2</sub><sup>-</sup> and/or •OH [18,19]. For instance, BiOCl nanosheets with oxygen vacancies were prepared for NO removal. The oxygen vacancies could trap the photogenerated electrons (e<sup>-</sup>), promoting charge separation. And compared with pristine BiOCl nanosheets, the reactive oxygen species referring to •O<sub>2</sub><sup>-</sup> and •OH were produced during the photocatalytic process, promoting the photocatalytic NO removal efficiency [20]. •OH (E<sup>0</sup>(•OH / H<sub>2</sub>O) = +2.38 V vs. NHE, E<sup>0</sup>(•O<sub>2</sub><sup>-</sup> / O<sub>2</sub>) = -0.33 V vs. NHE) with higher redox potential was favored for the degradation of contaminants. However, •O<sub>2</sub><sup>-</sup> was the general and primary active species during the photocatalytic process of BiOCl because of its limitation of the intrinsic layered structure, IEF, and band structure [9,10,12,21].

\* Corresponding authors.

E-mail addresses: [13875852619@163.com](mailto:13875852619@163.com) (S. Zhang), [Zhuyf@mail.tsinghua.edu.cn](mailto:Zhuyf@mail.tsinghua.edu.cn) (Y. Zhu).

<https://doi.org/10.1016/j.apcatb.2023.122642>

Received 25 November 2022; Received in revised form 11 March 2023; Accepted 13 March 2023

Available online 15 March 2023

0926-3373/© 2023 Elsevier B.V. All rights reserved.

To introduce a higher concentration of  $\bullet\text{OH}$  for efficient oxidation of contaminants, the synergetic heterogeneous photocatalytic-Fenton or photocatalytic-Fenton-like has been exploited by adding  $\text{H}_2\text{O}_2$  into a reaction solution containing Fe(II) in or doping Fe(III) into the catalysts. And then,  $\bullet\text{OH}$  was produced through the  $\text{H}_2\text{O}_2$  activation ( $\text{Fe}^{2+} + \text{H}_2\text{O}_2 \rightarrow \text{Fe}^{3+} + \bullet\text{OH} + \text{OH}^-$ ,  $k = 40 - 80 \text{ L} \cdot \text{mol}^{-1} \cdot \text{s}^{-1}$ ;  $\text{Fe}^{3+} + \text{H}_2\text{O}_2 \rightarrow \text{Fe}^{2+} + \bullet\text{O}_2 + 2\text{H}^+$ ,  $k = 0.01 - 0.02 \text{ L} \cdot \text{mol}^{-1} \cdot \text{s}^{-1}$ ) [22,23]. But,  $\bullet\text{OH}$  with the electrophilic feature is not strong enough to break the chemical bonds of aromatic rings, and is susceptible to the environments, causing low mineralization and deteriorated degradation efficiency of contaminants. Therefore, with the synergetic effect of  $\bullet\text{OH}$  and holes ( $\text{h}^+$ ) or  $\bullet\text{O}_2^-$ , the heterogeneous photocatalytic-Fenton performances for contaminants removal could be further improved [24,25]. For instance, Fe-doped BiOCl with oxygen vacancies were prepared as Fenton-like catalysts, which could convert the self-generated  $\text{H}_2\text{O}_2$  to massive  $\bullet\text{OH}$  for photodegradation of 2-chloro-4-nitrophenol. Meanwhile, the Fe-doped BiOCl also was beneficial to the charge separation, motivating the generation of  $\bullet\text{O}_2^-$  ( $\text{O}_2 + e^- \rightarrow \bullet\text{O}_2^-$ ). Such reactive oxygen species including  $\bullet\text{OH}$  and  $\bullet\text{O}_2^-$  played synergetic roles improved the photocatalytic performances of Fe-doped BiOCl (3.1 times), compared with pristine BiOCl [26].

In addition, the conversion rate from Fe(III) to Fe(II) is much lower, which is regarded as the rate-limiting step during the Fenton reaction process, resulting in Fe(III) accumulation and precipitation in the system ( $\text{Fe(III)} + 3\text{OH}^- \rightarrow \text{Fe(OH)}_3 \downarrow$ ). Thus, raising the conversion rate of Fe(III) to Fe(II) for Fe(III)/Fe(II) recycling during the Fenton reaction is a vital role to improve the oxidation of contaminants. Intrinsically, achieving Fe(III)/Fe(II) recycling is to receive electrons from the reaction or the environment, even from the catalysts. However, the electron donation from the catalysts is a discontinuous process because the electron-enriched solid catalyst is unstable. Additionally,  $\text{H}_2\text{O}_2$  is an inevitable role in the photocatalytic-Fenton process, but the activation efficiency of  $\text{H}_2\text{O}_2$  is low (<30 %) [27]. And the selective conversion of  $\text{H}_2\text{O}_2$  into  $\bullet\text{OH}$  is uncontrollable due to the oxidative activation process of  $\text{H}_2\text{O}_2$  ( $\text{Fe(III)} + \text{H}_2\text{O}_2 \rightarrow \text{Fe(II)} + \bullet\text{O}_2^- + 2\text{H}^+$ ) [27,28]. Herein, how to design catalysts with a sophisticated structure for promoted Fe(III)/Fe(II) recycling, selective and efficient activation of  $\text{H}_2\text{O}_2$ , improved catalysis activity and mineralization of phenolic pollutants is still an enormous challenge.

In this work, we rationally designed electron self-sufficient core-shell homo-structure BiOCl and Fe(III)-doped BiOCl (BiOCl@Fe-BiOCl) nanosheets for enhanced synergetic photocatalytic-Fenton performances of phenol removal. This electron self-sufficient structure was engaged by the IEF of the BiOCl core and electron capture center of doped-Fe in the Fe-BiOCl shell, expecting to be electron supplying and electron consumption, respectively. And the electron-captured Fe(III) should transit into Fe(II) rapidly, which should revert to Fe(III) for Fe(III)/Fe(II) recycling. The structure of BiOCl@Fe-BiOCl for the spatial transfer and separation of charge carriers was well-examined. And the Fe(III)/Fe(II) recycling, selectivity, and efficiency of  $\text{H}_2\text{O}_2$  activation, photocatalytic-Fenton activity, and mineralization of phenol over this catalyst also were investigated. We expected this work can provide novel inspiration for catalyst design and practical application of organic contaminant removal.

## 2. Experimental

### 2.1. Preparation of BiOCl@Fe-BiOCl, BiOCl, BiOCl-Fe, and FeOCl nanosheets

The core-shell BiOCl@Fe-BiOCl nanosheets were prepared through the solution evaporation-calcination method.  $\text{Bi(NO}_3)_3 \cdot 5\text{H}_2\text{O}$  (2 mmol) was dissolved into 1 mL of ethylene glycol (EG) to form a transparent solution. And, KCl (2 mmol) and  $\text{FeCl}_3$  (1 mmol) were dissolved into 1 mL of water, which was rapidly dumped into the  $\text{Bi(NO}_3)_3 \cdot 5\text{H}_2\text{O}$  solution to form a white suspension. Then, this suspension was heated up at

80 °C for 4 h to remove the solvent. During this process, the color of the suspension was changed from white to light yellow, and golden. Subsequently, these resultants were calcinated at 230 °C for 4 h by the heating rate of 10 °C/min. After cooling down naturally, the resultants were collected, washed, and dried for further application, and the products were designated as BiOCl@Fe-BiOCl. Similarly, the BiOCl nanosheets were prepared through the above process but without adding  $\text{FeCl}_3$ . Comparatively, another BiOCl nanosheets were prepared only in the presence of  $\text{FeCl}_3$  through the above process but without introducing KCl, which was labeled as BiOCl-Fe. While the resulting FeOCl was prepared by direct calcination  $\text{FeCl}_3$  at 230 °C for 4 h.

### 2.2. Characterization

The X-ray diffractometer (Rigaku) was used to measure the powder X-ray diffraction (XRD) patterns of all samples. Scanning electron microscopy (SEM, Hitachi SU-8010) and transmission electron microscopy (TEM, Hitachi HT7700) with elemental mapping was used to record the TEM, high-resolution TEM (HRTEM) images and selected area electron diffraction (SAED) patterns of products. Kelvin probe force microscope (KPFM) technique and atomic force microscopy (AFM) images for different samples were conducted on Multiple Single-Molecule Force Spectroscopy (Cypher VRS, Oxford Instruments). UV-vis diffuse reflectance spectra (DRS) of the resulting products were performed on a UV-Vis spectrophotometer (Hitachi U-3900). Raman Microscope (LabRAM HR, Jobin Yvon) with an excitation wavelength of 632.8 nm was employed to record the Raman shifts of different samples. Thermo Fisher Spectroscopy (Escalab 250 Xi) was used to record the X-ray photoelectron spectroscopy (XPS) of some samples. A fluorescence spectrophotometer (Edinburgh F900) with an excitation wavelength of 295 nm was used to record the photoluminescence (PL) spectra. And the time-resolved transient PL (TRT-PL) spectroscopy of different samples was performed on a fluorescence spectrophotometer (Edinburgh, FLS1000). The surface photovoltage (SPV) measurements were conducted with a home-built instrument as previously reported [29]. The reactive oxygen species of  $\bullet\text{O}_2^-$  and  $\bullet\text{OH}$  were detected by electron paramagnetic resonance (EPR, JNM-ECZ600R) technique. For this detection, 5,5-dimethyl-1-pyrroline N-oxide (DMPO) was used. And,  $\text{DMPO} \cdot \bullet\text{O}_2^-$  and  $\text{DMPO} \cdot \bullet\text{OH}$  were measured in methanol and aqueous solution, respectively. Electrochemical characterizations of the resultants including Mott-Schottky (MS) plot, electrochemical impedance spectroscopy (EIS), and photocurrent measurement were performed on the electrochemical workstation (CHI 660E, China) in a 0.5 M  $\text{Na}_2\text{SO}_4$  solution.

### 2.3. Photocatalytic and photocatalytic-Fenton activity

The photocatalytic performances of different samples were evaluated by photodegrading the phenol solution, and a Xenon lamp (300 W) with or without a 420 nm cut-off filter was selected as visible light or full-spectra light, respectively. Typically, 20 mg of resulting photocatalysts were dispersed in a phenol solution (10 mg/L, 50 mL) ultrasonically to form a suspension. This suspension was stirred in the dark for 1 h to achieve equilibrium of adsorption-desorption before the light turned on. During the light irradiation process, 2 mL of aliquots were withdrawn from reacted suspension at each fixed interval. The catalysts were removed from the withdrawn suspension by employing 0.22  $\mu\text{m}$  Millipore filters, and the concentration of the resulting transparent solution was analyzed on High-Performance Liquid Chromatography (HPLC, Prominence, Shimadzu). The photocatalytic-Fenton performances of different samples were also carried out by following the above procedure, but just adding 10  $\mu\text{L}$  of  $\text{H}_2\text{O}_2$  (30 %, 2.58 mmol/L) after adsorption-desorption equilibrium.

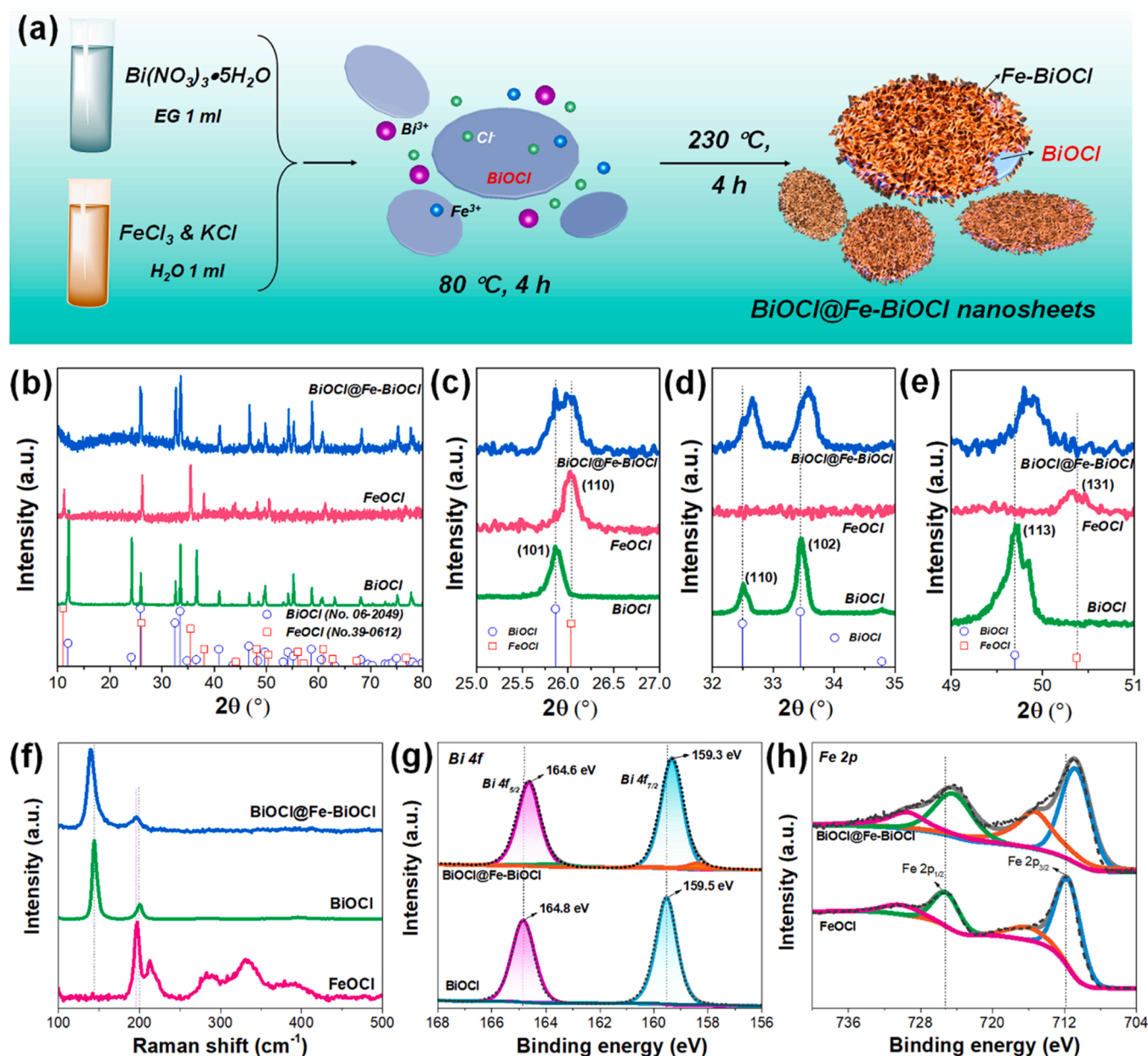


**Fig. 1.** (a) Scheme illustration of core-shell BiOCl@Fe-BiOCl nanosheets synthesis, (b) XRD patterns of different products, and corresponding partial magnified XRD patterns in the different regions, (c)  $25\text{--}27^\circ$ , (d)  $32\text{--}35^\circ$ , (e)  $49\text{--}51^\circ$ . (f) Raman spectra, high-resolution of (g) Bi 4f, (h) Fe 2p spectra of different samples.

## 2.4. Computational details

### 2.4.1. Band structure calculation

The present first principle DFT calculations are performed by Vienna Ab initio Simulation Package (VASP) with the projector augmented wave (PAW) method [30,31]. The exchange-functional is treated using the generalized gradient approximation (GGA) of the Perdew-Burke-Ernzerhof (PBE) function [32]. The energy cut-off for the plane wave basis expansion was set to 450 eV and the force on each atom less than 0.02 eV/Å was set for the convergence criterion of geometry relaxation. A 15 Å vacuum was added along the z direction to avoid the interaction between periodic structures for both single-layer BiOCl and Fe-doped BiOCl. The Brillouin zone integration was performed using  $5 \times 5 \times 1$  k-point sampling for pristine BiOCl and Fe-doped BiOCl. The self-consistent calculations apply a convergence energy threshold of  $10^{-5}$  eV.

### 2.4.2. Adsorption energy calculation

All the calculations were performed in the framework of the density functional theory with the projector-augmented plane-wave method, as implemented in the VASP [33]. The generalized gradient approximation of the PBE function was selected for the exchange-correlation potential [34]. The van der Waals interaction was described by the DFT-D3 approach [35]. The cut-off energy for the plane wave was set to 400 eV. The energy criterion was set to  $10^{-5}$  eV in the iterative solution of the Kohn-Sham equation. A vacuum layer of 15 Å was added perpendicular to the sheet to avoid artificial interaction between periodic images. The Brillouin zone integration was performed using a  $2 \times 2 \times 1$  K-mesh. All the structures were relaxed until the residual forces on the atoms declined to less than  $10^{-4}$  eV/Å.



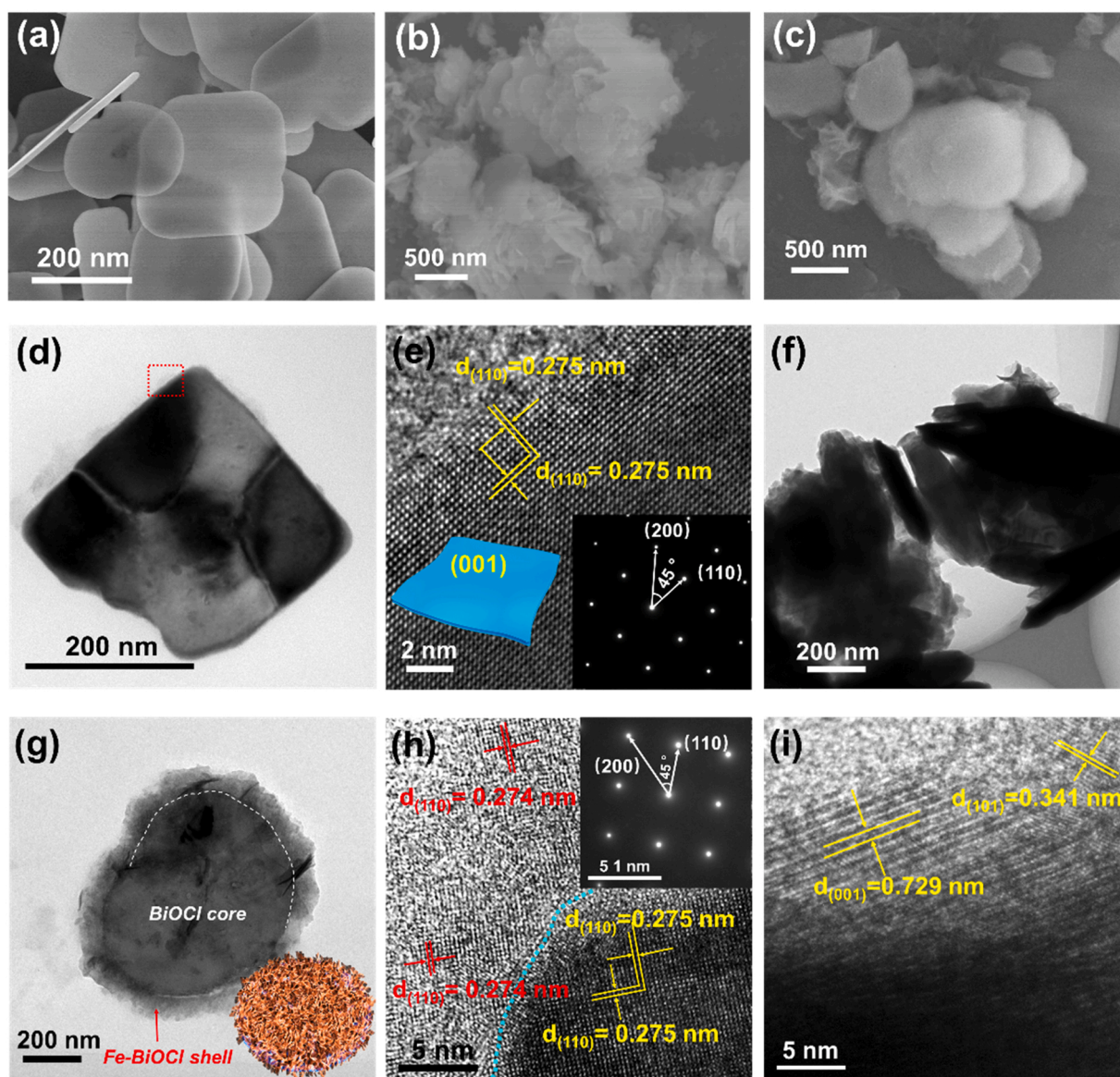


**Fig. 2.** SEM images of (a) BiOCl, (b) FeOCl, (c) BiOCl@Fe-BiOCl. (d) TEM, (e) HRTEM images of BiOCl (inset with SAED pattern). (f) and (g) TEM images of BiOCl@Fe-BiOCl, (h) HRTEM, and (i) lateral HRTEM images of BiOCl@Fe-BiOCl (inset with SAED pattern).

### 3. Results and discussion

#### 3.1. Core-shell BiOCl@Fe-BiOCl nanosheets

The electron self-sufficient core-shell BiOCl@Fe-BiOCl nanosheets were prepared through a combined method of solvent-evaporation and calcination, as illustrated in Fig. 1a. The characteristic peaks of resulting BiOCl and FeOCl were well-indexed to tetragonal BiOCl (JCPDS No. 06–2049) and FeOCl (JCPDS No. 39–0612), respectively (Fig. 1b). In terms of core-shell BiOCl@Fe-BiOCl nanosheets, all the characteristic peaks of were also identical to BiOCl (JCPDS No. 06–2049). However, compared to the XRD patterns of BiOCl, after magnifying the XRD patterns, it was noticed that partial characteristic peaks were shifted to higher  $2\theta$ . For instance, in the  $2\theta$  regions of 25–27°, the (101) planes of BiOCl were shifted to higher  $2\theta$  for BiOCl@Fe-BiOCl, which even were closer to the (110) planes of FeOCl (Fig. 1c). Furthermore, such up-shifted characteristic peaks of BiOCl@Fe-BiOCl were also observed in its other regions of XRD patterns and XRD patterns of Fe-doped BiOCl (Fig. 1d–e, Fig. S1). Whereas, the characteristic peaks of FeOCl were barely observed in this XRD pattern owing to its high solubility. Such up-

shifted characteristic peaks of BiOCl@Fe-BiOCl indicated that the crystal lattices of BiOCl were shrank due to the smaller radius of doped Fe [36]. Additionally, the elemental mapping of BiOCl@Fe-BiOCl also demonstrated that the Fe was doped into BiOCl successfully (Fig. S2).

For the Raman spectrum of BiOCl nanosheets (Fig. 1f), two significant characteristic peaks at 144 and 199  $\text{cm}^{-1}$  assigned to  $A_{1g}$  external stretching mode and  $E_g$  internal stretching mode of Bi–Cl band were observed, respectively [37,38]. As regards to FeOCl, a series of peaks located at 197.1  $\text{cm}^{-1}$ , 213.2  $\text{cm}^{-1}$ , and 281  $\text{cm}^{-1}$ , 331.5  $\text{cm}^{-1}$  corresponding to Fe–Cl and Fe–O bands were observed [39,40]. For the BiOCl@Fe-BiOCl nanosheets, the characteristic peaks assigned to FeOCl were scarcely detected, demonstrating that the Fe was doped into BiOCl rather than forming FeOCl on the BiOCl surface. And characteristic peaks ascribed to Bi–Cl bands stretching mode of BiOCl were observed, but these two peaks were respectively blue-shifted by  $\sim 4 \text{ cm}^{-1}$  to 140 and 195  $\text{cm}^{-1}$  due to the Fe doping (Fig. 1f). Furthermore, due to the Fe doping, the surface defects of BiOCl@Fe-BiOCl were detected (Fig. S3).

In the Bi 4f spectra, two peaks centered at 164.8 and 159.5 eV respectively ascribed to Bi 4f<sub>5/2</sub> and Bi 4f<sub>7/2</sub> were observed for BiOCl nanosheets [38]. Comparatively, these peaks were down-shifted by



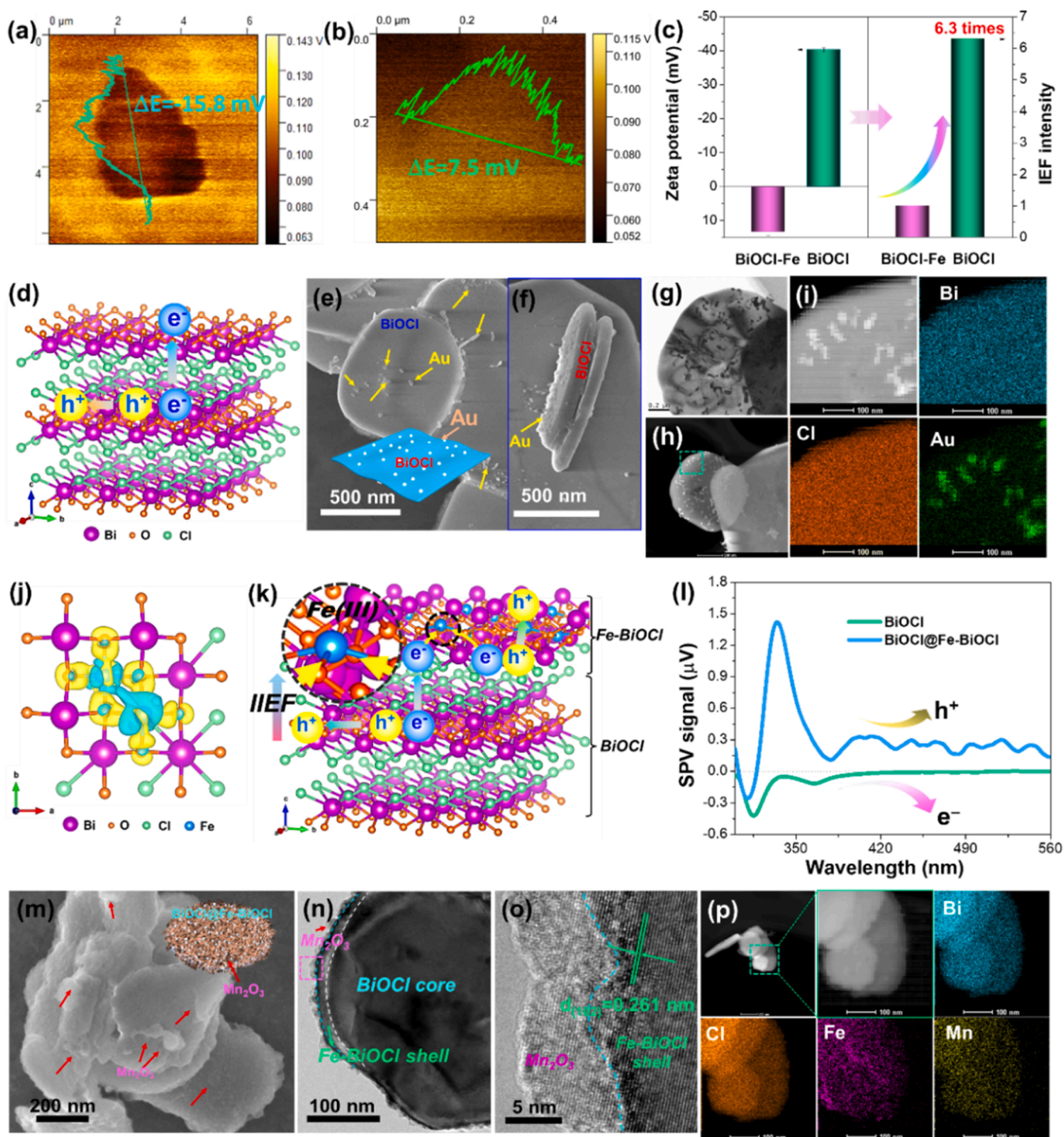


**Fig. 3.** Surface potential of (a) BiOCl, (b) BiOCl-Fe, (c) Zeta potential and corresponding internal electric field intensity comparison of BiOCl and BiOCl-Fe. (d) The charge transfer illustration of BiOCl. Photo-deposition of Au particles on BiOCl nanosheets, (e) top-view and (f) lateral-view SEM images. (g) TEM, (h) bright field TEM, (i) magnified bright-field TEM images of (h) and corresponding elements mapping of Au deposited on BiOCl. (j) Charge density differences of Fe-BiOCl (Yellow and blue iso-surfaces depict charge accumulation and charge depletion, respectively). (k) Charge transfer illustration of BiOCl@Fe-BiOCl. (l) SPV spectra of different samples. (m) SEM, (n) TEM, (o) HRTEM, (p) bright-field TEM images of  $\text{Mn}_2\text{O}_3$  particles deposited on BiOCl@Fe-BiOCl nanosheets.

$\sim 0.2$  eV to lower binding energies of 164.6 and 159.3 eV for core-shell BiOCl@Fe-BiOCl nanosheets probably due to the electron-trapped surface oxygen vacancies (Fig. 1g), which was redistributed to  $\text{Bi}^{3+}$  [21]. In the Fe 2p spectra of FeOCl nanosheets, two peaks located at 711.6 and 725.1 eV with satellite peaks respectively ascribed to the Fe  $2p_{3/2}$  and Fe  $2p_{1/2}$  were observed, implying that Fe in FeOCl is  $\text{Fe}^{3+}$  state [39]. Compared to FeOCl nanosheets, the resulting Fe  $2p_{3/2}$  and Fe  $2p_{1/2}$  of

BiOCl@Fe-BiOCl nanosheets were also shifted by  $\sim 0.4$  eV to lower binding energy due to the redistributed electrons, suggesting that the Fe in this structure could be formed  $\text{Fe}^{2+}$  easily (Fig. 1h). Such down-shifted binding energy of Bi 4f and Fe 2p suggested that its charge density and oxidation states may affect the subsequent Fe(III)/Fe(II) recycling and  $\text{H}_2\text{O}_2$  activation process.

The as-prepared BiOCl showed sheet-like morphology with smooth

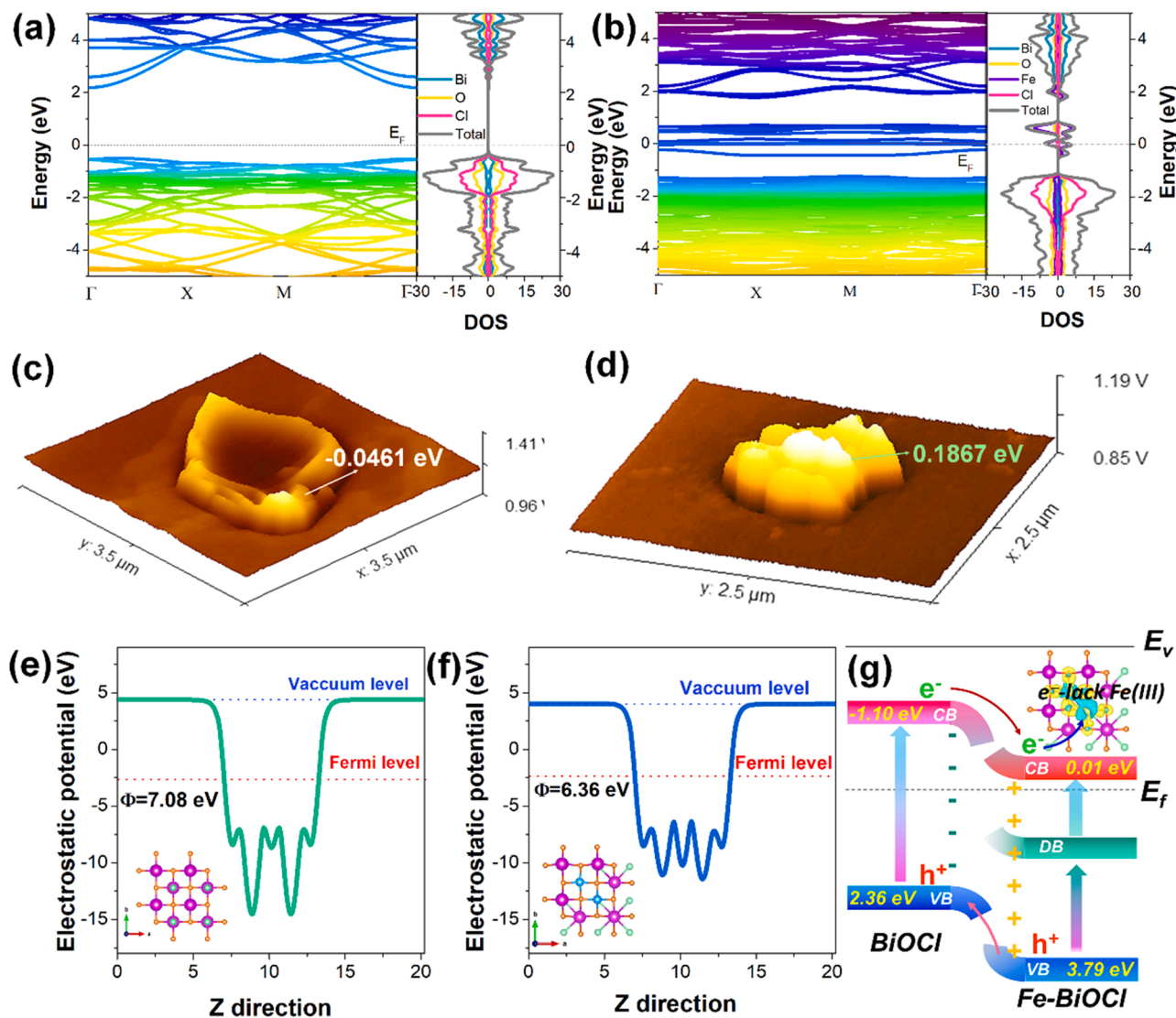


**Fig. 4.** Band structure calculation and DOS of (a) BiOCl and (b) Fe-BiOCl. The surface potential of (c) BiOCl and (d) BiOCl@Fe-BiOCl detected with KPFM, work function calculation of (001) facet of (e) BiOCl and (f) BiOCl@Fe-BiOCl. (g) Band structures and charge transfer of BiOCl@Fe-BiOCl.

surface (Fig. 2a, d, Fig. S4a and S4c), and FeOCl showed aggregated and irregular nano-scale sheet-like morphology (Fig. 2b). The resulting BiOCl@Fe-BiOCl also exhibited round-sheet-like morphology but with rough surface (Fig. 2c and Fig. 2f-g). And the core-shell BiOCl@Fe-BiOCl nanosheets with a clear boundary between the core and shell could be observed through the TEM images (Fig. 2g, Fig. S4e-S4f). In the corresponding HRTEM images of BiOCl nanosheets, clear interplanar lattice fringes spacing of 0.275 nm assigned to (110) atomic planes of BiOCl were observed (Fig. 2e and Fig. S4b). Furthermore, the clear SAED patterns and lateral lattice spacing of 0.738 nm assigned to (001) atomic planes of BiOCl demonstrated that the resulting BiOCl nanosheets were enclosed with (001) facet predominantly (Fig. 2e, Fig. S4c-S4d) [12,16,41]. For the inner core of BiOCl@Fe-BiOCl nanosheets, the clear and continuous interplanar lattice fringes spacing of 0.275 nm assigned to (110) atomic planes of BiOCl and SAED patterns were observed (Fig. 2h and Fig. S4g), demonstrating the existence of BiOCl core and the BiOCl core was also enclosed with (001) facet primarily [8,12,16,41]. Simultaneously, the slightly shrank lattice fringes spacing of 0.274 nm, and lateral lattices spacing of 0.728 nm respectively assigned to (110), (200), and (001) atomic planes of BiOCl confirmed the slight shrank structure of Fe-BiOCl shell due to the Fe doping (Fig. 2h-i, and Fig. S4h, Fig. S5). Furthermore, because of the doped Fe for the defective band [9,

13,24], the light response of electron self-sufficient core-shell BiOCl@Fe-BiOCl nanosheets were broadened to the whole violet-visible region, compared to the limited violet region of BiOCl nanosheets (Fig. S6).

### 3.2. Electron self-sufficient core-shell BiOCl@Fe-BiOCl nanosheets for spatial separation of charge carriers

Based on previous research [42–45], the unique layered structure of BiOX could establish IEF easily for spatial transfer and efficient separation of charge carriers. Thus, the IEF of BiOCl was investigated based on the Zeta potential and surface potential [43,46–48]. The surface potential of BiOCl nanosheets was -15.8 mV (Fig. 3a, Fig. S7), and its Zeta potential was -40.3 mV (Fig. 3b). On the other hand, another BiOCl nanosheets, labeling as BiOCl-Fe (prepared by only adding  $\text{FeCl}_3$ ), presented the lower and positive surface potential of 7.5 mV. Based on the corresponding Zeta potential, the IEF intensity of BiOCl nanosheets was 6.3 times higher than that of BiOCl-Fe (Fig. 3c). Such strong IEF of BiOCl probably drives the efficient charge transfers and separation. For the general BiOCl with primary (001) facets exposure and  $[\text{Bi}_2\text{O}_2]^{2+}$  termination [21], the photogenerated  $e^-$  should be driven to the predominant (001) exposure facets by the strong IEF (Fig. 3d), resulting in



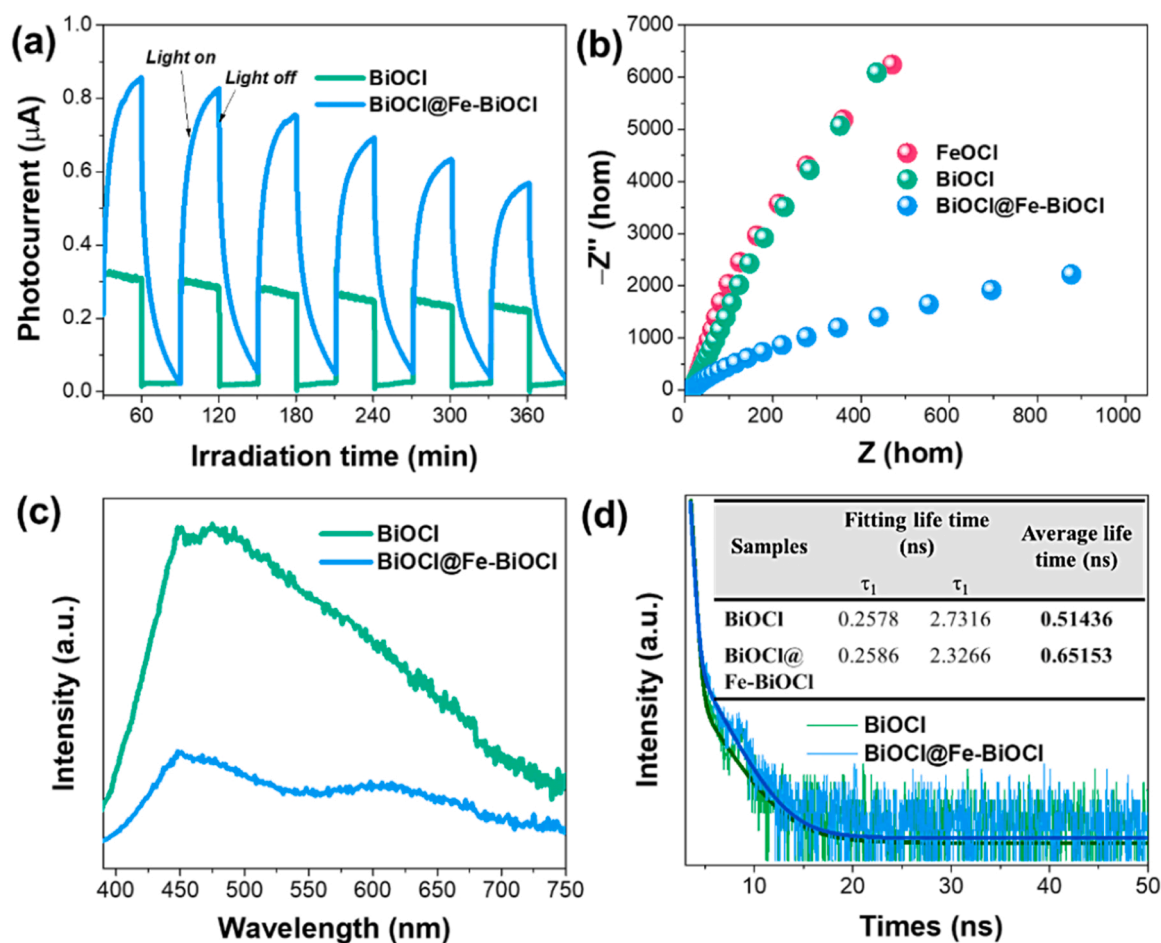


Fig. 5. (a) Photocurrents, (b) EIS, (c) PL spectra, and (d) time-resolved PL spectra of different samples.

abundant  $e^-$  accumulation on the surface of BiOCl. Contrarily,  $h^+$  transfer to the lateral facets of BiOCl. Then, the photo-deposition tests were carried out by depositing Au and  $\text{Mn}_2\text{O}_3$  on its surface through electrons reduction and holes oxidation, respectively (Fig. S8e-i, Fig. S8). According to the SEM and TEM images of Au deposition (Fig. 3e-f, Fig. S8a), particles deposited primarily on the (001) exposure facets of BiOCl were observed. Then, the TEM, bright field TEM images and corresponding elemental mapping of this sample validated that the deposited particles were Au (Fig. 3g-i). On the other hand, few  $\text{Mn}_2\text{O}_3$  particles deposited on the lateral edge of BiOCl were observed (Fig. S8b-S8e), consistent with the above assumption. All these results demonstrated that the surface of BiOCl was enriched with electrons.

Compared to the regular tetragonal BiOCl, the Fe-BiOCl exhibited slight structure distortion that the shortened length of Bi-O bonds was observed due to the smaller radius of doped Fe(III) (Fig. 3j, Fig. S9). Furthermore, the charges of doped Fe(III) are inclined to dissipate around, and then accumulate at O atoms, resulting in the electron-capture centers of Fe atoms (Fig. 3j). In the core-shell BiOCl@Fe-BiOCl nanosheets, the surface-enriched  $e^-$  of inner BiOCl core could act as electron supplier for the electron-capture centers of Fe(III) in the Fe-BiOCl shell, transiting Fe(III) to Fe(II). And the Fe(III) capturing the electrons for charge density increasing was confirmed by the in-situ XPS under light irradiation (Fig. S10). Then, the surface-enriched electrons are eliminated, establishing the electrons self-sufficient structure in the core-shell BiOCl@Fe-BiOCl nanosheets. Whereas, the photogenerated  $h^+$  in BiOCl and Fe-BiOCl will transfer to the lateral surface of BiOCl and the surface of Fe-BiOCl, respectively (Fig. 3k), accumulating holes on the surface of resulting BiOCl@Fe-BiOCl. The SPV spectra were used to examine the charge transfer directions of BiOCl and BiOCl@Fe-BiOCl. As

showed in Fig. 3l, the predominant positive SPV signal of BiOCl@Fe-BiOCl nanosheets was observed, indicating that  $h^+$  migrated to the surface. Contrarily, the primary negative SPV signal of BiOCl demonstrated that the  $e^-$  could be driven to the surface under the strong IEF. These results were consistent with the above-mentioned hypothesis. Furthermore, the hole-enriched surface of BiOCl@Fe-BiOCl nanosheets was verified by the photo-deposition tests of  $\text{Mn}_2\text{O}_3$  and Au [49]. Compared to pristine BiOCl@Fe-BiOCl nanosheets, the  $\text{Mn}_2\text{O}_3$  deposited BiOCl@Fe-BiOCl nanosheets showed rougher surface, and obvious deposited particles were observed (Fig. 3m). Furthermore, the particles deposited on the core-shell BiOCl@Fe-BiOCl nanosheets were also observed according to the TEM images (Fig. 3n, Fig. S8f-S8g, Fig. S8h). And elements mapping (Fig. 3p), the clear lattices fringes of 0.251 nm and 0.261 nm respectively assigned to (110) atomic planes of  $\text{Mn}_2\text{O}_3$  and (102) planes of BiOCl in the HRTEM images also confirmed that the  $\text{Mn}_2\text{O}_3$  particles almost covered the surface of BiOCl@Fe-BiOCl nanosheets due to its surface enriched holes (Fig. 3o, Fig. S8i). On the contrary, only a few Au particles deposited on the surface of BiOCl@Fe-BiOCl nanosheets (Fig. S8j-S8k), further verifying the hole-enriched surface of BiOCl@Fe-BiOCl nanosheets. Herein, in the electron self-sufficient core-shell BiOCl@Fe-BiOCl nanosheets, the IEF of the BiOCl core drove the electrons to its surface as electrons supplying, which were further captured and consumed by the electron-capture centers of doped Fe(III) for in the Fe-BiOCl shell Fe(II) transition. As such, an electron self-sufficient structure was constructed in the core-shell BiOCl@Fe-BiOCl nanosheets, separating charge carriers spatially and efficiently.

On the other hand, the band structure alignments of the core-shell BiOCl@Fe-BiOCl nanosheets for the charge separation



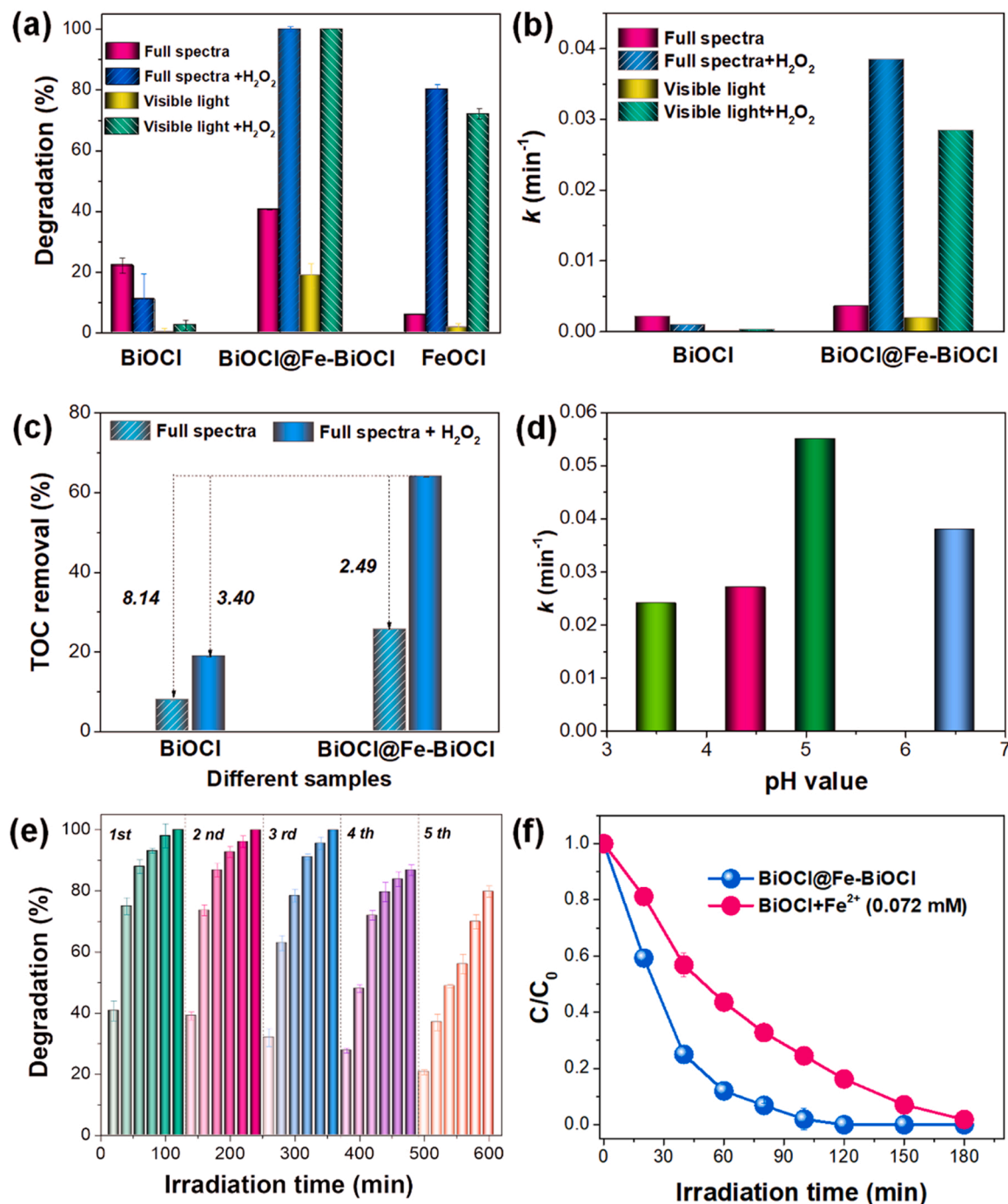


**Fig. 6.** (a) Photocatalytic and photocatalytic-Fenton performances comparison, and (b) reaction rate constant comparison of different samples without and with H<sub>2</sub>O<sub>2</sub> under full spectra and visible light (pH = 6.5). (c) TOC removal comparison of BiOCl and BiOCl@Fe-BiOCl. (d) The reaction rate of BiOCl@Fe-BiOCl at different pH values. (e) Photocatalytic cycling of BiOCl@Fe-BiOCl. (f) Comparison of photocatalytic-Fenton performances of BiOCl@Fe-BiOCl and BiOCl in the presence of Fe<sup>2+</sup> (0.072 mM).

thermodynamically were also investigated. The band structure and corresponding density of states (DOS) of BiOCl suggested that the BiOCl was an indirect semiconductor with a wide  $E_g$  of 3.46 eV (Fig. 4a and Table S1). Comparatively, the  $E_g$  of Fe-BiOCl was narrowed to 3.01 eV, wide intermediated defective band (DB) was generated between the bottom of the conduction band (CB) and the top of the valence band (VB) due to Fe doping (Fig. 4b). Furthermore, the charge density of the Fe-BiOCl is much higher than that of pristine BiOCl.

The work function (WF) of BiOCl nanosheets and BiOCl@Fe-BiOCl nanosheets were measured by the in-situ KPFM under N<sub>2</sub> ambience by

employing highly oriented pyrolytic graphite (HOPG) as reference tip. The average contact potential difference (CPD) of BiOCl nanosheets and BiOCl@Fe-BiOCl nanosheets are -0.0543 V and 0.1826 V, respectively (Fig. 4c-d, and Fig. S11). Then, the WF can be calculated by following the formula WF (eV) = 4.35 +  $e \times$  CPD (where 4.35 eV is the WF of the corrected probe (HQ NSC18/Pt), and  $e$  is the charge of an electron) [50]. Therefore, the WF of BiOCl nanosheets and BiOCl@Fe-BiOCl can be determined to be 4.40 eV and 4.17 eV, respectively (Fig. 4c and d). These measured values suggested that the higher WF level of the Fe-BiOCl shell could raise the WF of BiOCl@Fe-BiOCl. However, the WF

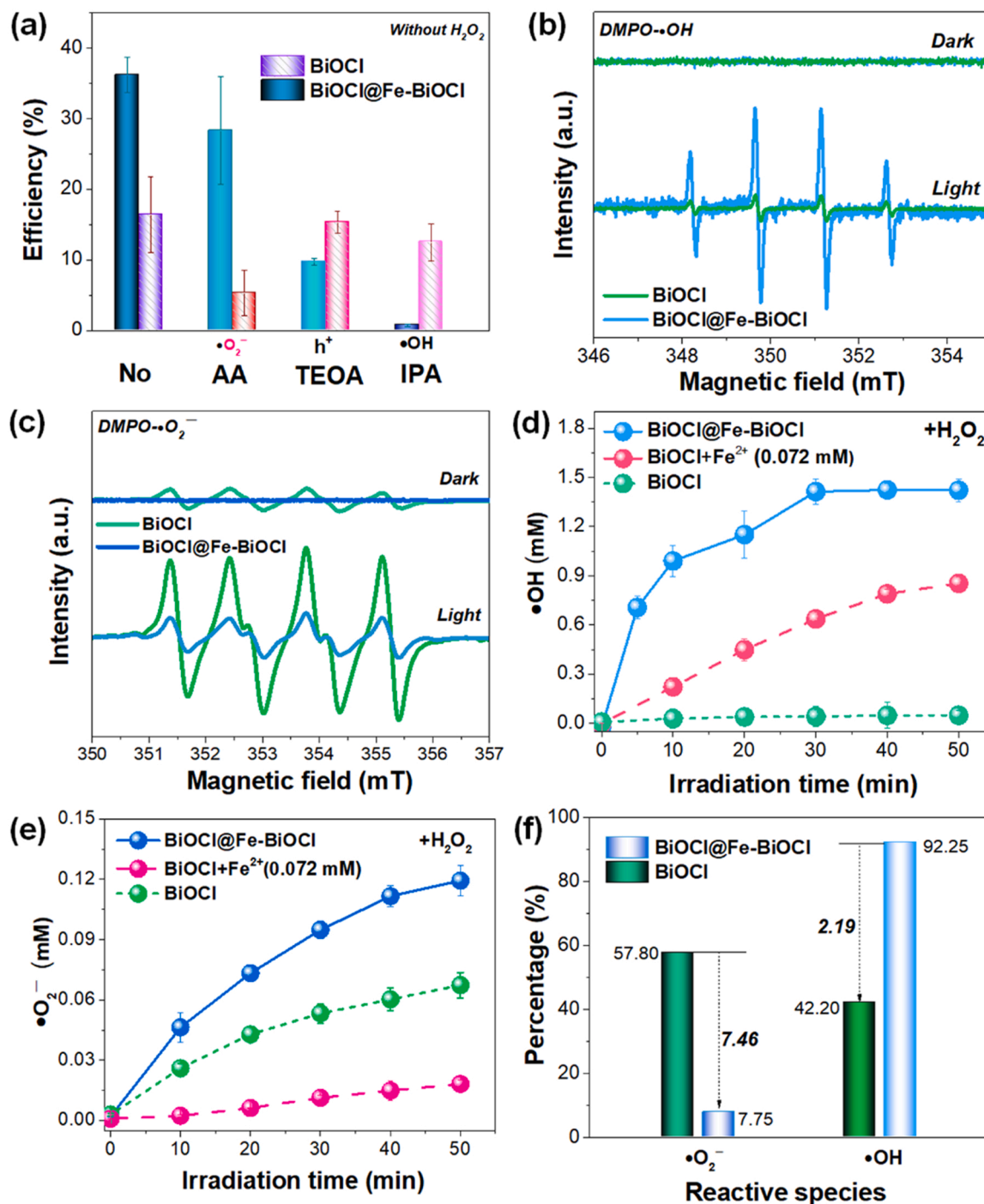


**Fig. 7.** (a) Scavenger tests comparison of BiOCl and BiOCl@Fe-BiOCl. (b) DMPO-•OH and (c) DMPO-•O<sub>2</sub><sup>-</sup> EPR spectra of BiOCl@Fe-BiOCl and BiOCl. (d) •OH and (e) •O<sub>2</sub><sup>-</sup> concentration comparison during the photocatalytic-Fenton process. (f) •OH and •O<sub>2</sub><sup>-</sup> selectivity comparison of different samples.

of Fe-BiOCl is unable to measure. Therefore, the WF of (001) facets BiOCl and Fe-BiOCl were calculated (Fig. 4e-4f). The Fe-BiOCl possesses a higher WF of 6.36 eV, which is 0.72 eV higher than that of BiOCl (7.08 eV). Thus, the WF value of the Fe-BiOCl shell should be 3.68 eV, as combined with the measured value. After contacting, the band edge of Fe-BiOCl should bend upward, and the BiOCl should bend downward contrarily, resulting in hole-enriched and electron-enriched at the interface correspondingly. As combined the band structure and WF of BiOCl and Fe-BiOCl (Fig. S12a-S12c), the charge transfer of BiOCl@Fe-BiOCl nanosheets during the photocatalytic process should follow the Type-II pathway (Fig. 4g, Fig. S12d). As a result, theoretically,

the charge carriers of BiOCl@Fe-BiOCl nanosheets could be separated easily and efficiently [51,52].

The charge separation of these core-shell BiOCl@Fe-BiOCl nanosheets was further examined by photocurrent, EIS, steady-state PL, and TRT-PL spectroscopy (Fig. 5). Compared with pristine BiOCl nanosheets, the core-shell BiOCl@Fe-BiOCl nanosheets exhibited higher photocurrent intensity, revealing the superior charge separation dynamics (Fig. 5a) [10,12]. Meanwhile, the core-shell BiOCl@Fe-BiOCl nanosheets also showed the lowest PL intensity and smallest EIS radius, indicating that the charge recombination could be suppressed (Fig. 5b and c). Furthermore, the longer lifetime of charge carriers in the

core-shell BiOCl@Fe-BiOCl nanosheets also revealed its higher charge separation efficiency (Fig. 5d, Table S2) [15,38]. Based on the above-mentioned results and discussions, the charge transfer and separation of the core-shell BiOCl@Fe-BiOCl nanosheets were enhanced by the intrinsic electron self-sufficient structure and its band alignment.

### 3.3. Electron self-sufficient core-shell BiOCl@Fe-BiOCl nanosheets boosting Fe(III)/Fe(II) recycling, $H_2O_2$ activation, photocatalytic-Fenton performances

The photocatalytic and synergetic photocatalytic-Fenton performances of electron self-sufficient core-shell BiOCl@Fe-BiOCl nanosheets were examined under full spectra and visible light irradiation, as compared to BiOCl and FeOCl (Fig. 6a, Fig. S13a-S13f). In the absence of  $H_2O_2$ , the FeOCl was almost unable to degrade the phenol, the BiOCl could achieve ~30 % photodegradation efficiency within 180 min under full spectra. While the BiOCl@Fe-BiOCl nanosheets could improve the phenol photodegradation efficiency to 50 % (Fig. 6a). Interestingly, the phenol degradation efficiencies of BiOCl@Fe-BiOCl nanosheets and FeOCl were boosted through the synergetic photocatalytic-Fenton reaction in the presence of  $H_2O_2$  (2.58 mmol/L, pH = 6.5). The degradation efficiency of FeOCl could reach ~80 % within 180 min, and the degradation efficiency of core-shell BiOCl@Fe-BiOCl nanosheets were achieved at almost 100 % within 100 min (Fig. 6a, Fig. S13a-S13b). Furthermore, the core-shell BiOCl@Fe-BiOCl nanosheets also exhibited superior synergetic photocatalytic-Fenton performances under visible light irradiation (Fig. 6a, Fig. S13c-S13b). The photocatalytic-Fenton reaction rate constant ( $k$ ,  $\text{min}^{-1}$ ) of core-shell BiOCl@Fe-BiOCl nanosheets under full spectra was ~41.32 and ~2.67 times than that of BiOCl and FeOCl, respectively (Fig. 6b, Fig. S13e). And under visible light irradiation, the BiOCl@Fe-BiOCl nanosheets also showed superior photocatalytic-Fenton performances (Fig. S13f).

Notably, the core-shell BiOCl@Fe-BiOCl nanosheets also showed excellent mineralization ability that ~64 % TOC removal rate was obtained within 90 min with the assistance of synergetic photocatalytic-Fenton, coinciding with its photocatalytic or photocatalytic-Fenton performances (Fig. S14a). And this TOC removal efficiency of core-shell BiOCl@Fe-BiOCl nanosheets through synergetic photocatalytic-Fenton reaction was ~2.84 times higher than that only through photocatalytic reaction. Moreover, such TOC removal efficiency of core-shell BiOCl@Fe-BiOCl nanosheets also was ~7.02 times than that of BiOCl (Fig. 6c). This outstanding TOC removal rate of core-shell BiOCl@Fe-BiOCl nanosheets revealed its remarkable mineralization ability. Additionally, the core-shell BiOCl@Fe-BiOCl nanosheets showed superior synergetic photocatalytic-Fenton activities at a pH value of 5.1 that complete degradation of phenol could be achieved within 60 min (Fig. S14b). And its  $k$  value was  $0.055 \text{ min}^{-1}$ , which was ~2.29 times than that obtained at pH = 3.5 (Fig. 6d). Furthermore, the BiOCl@Fe-BiOCl nanosheets exhibited superior stability according to the photocatalysis recycling tests and comparison of used photocatalysts (Fig. 6e, Fig. S14c). After the photocatalytic-Fenton reaction, the phase, morphology, and elements chemical states of core-shell BiOCl@Fe-BiOCl nanosheets were barely tailored, also demonstrating its higher stability (Fig. S15). Additionally, BiOCl in the presence of  $Fe^{2+}$  (0.072 mmol/L) for photocatalytic-Fenton reaction were used to compare (Fig. 6f). At high concentration of  $Fe^{2+}$ , its photocatalytic-Fenton performances were still inferior to that of BiOCl@Fe-BiOCl within 180 min. Compared with previous related studies (Tables S3) [25,26,53], the BiOCl@Fe-BiOCl nanosheets also showed higher photocatalytic-Fenton performances.

During this photocatalytic process of core-shell BiOCl@Fe-BiOCl nanosheets and BiOCl nanosheets, the reactive species were investigated by EPR spectra and scavenger tests (Fig. 7a-7c, Fig. S16). Based on the scavenger tests, the predominant reactive specie for BiOCl nanosheets was  $\bullet O_2^-$ , and then was  $\bullet OH$  during the photocatalytic process. The remarkable higher DMPO- $\bullet O_2^-$  signal and weak DMPO- $\bullet OH$  signal for

BiOCl under light irradiation further verified that  $\bullet O_2^-$  was the primary reactive species (Fig. 7b-7c). On the contrary, the primary reactive species for BiOCl@Fe-BiOCl nanosheets were  $\bullet OH$  and  $h^+$ ,  $\bullet O_2^-$  was the ignorable role (Fig. 7a and Fig. S16). The distinctive strong DMPO- $\bullet OH$  signal and scarcely observed DMPO- $\bullet O_2^-$  signal of BiOCl@Fe-BiOCl nanosheets generated under light illumination further confirmed this point (Fig. 7b-7c). These results demonstrated that the  $e^-$  of BiOCl nanosheets transferred to its surface and formed  $\bullet O_2^-$  as reactive species. Comparatively, surface  $h^+$  enrichment and corresponding generated  $\bullet OH$  were the predominant reactive specie for BiOCl@Fe-BiOCl nanosheets during the photocatalytic process.

Then, the concentration variations of  $\bullet OH$  and  $\bullet O_2^-$  during the synergetic photocatalytic-Fenton process were also examined by using the benzoic acid and nitroblue tetrazolium as molecule probes, respectively (Fig. 7d-e, and Fig. S17). As shown in Fig. S17a, as the primary active species for BiOCl@Fe-BiOCl, the  $\bullet OH$  accumulated concentration during the synergetic photocatalytic-Fenton process was gradually increased, which was much higher than that during the photocatalytic process, the photocatalytic process of BiOCl or its photocatalytic-Fenton reaction (Fig. 7d). This result revealed that the  $H_2O_2$  was activated and converted into  $\bullet OH$  through Fenton reaction ( $Fe^{2+} + H_2O_2 \rightarrow Fe^{3+} + \bullet OH + OH^-$ ), in the presence of the unique electron self-sufficient structure of core-shell BiOCl@Fe-BiOCl nanosheets. Simultaneously, the Fe(III)/Fe(II) recycling was also facilitated via the Fenton reaction and photocatalytic process. That was, the doped Fe(III) of the Fe-BiOCl shell captured electrons, which were driven by the strong IEF of the BiOCl core, transiting Fe(III) to Fe(II) during the photocatalytic process. Then, the Fe(II) transited back to Fe(III) state through the Fenton reaction. As the photocatalytic-Fenton reaction proceeded, the Fe(III)/Fe(II) recycling could conduct persistently. Compared with  $\bullet OH$  concentration, the  $\bullet O_2^-$  production during the photocatalytic-Fenton process of BiOCl@Fe-BiOCl, or photocatalytic and photocatalytic-Fenton process of BiOCl was much lower (Fig. S17b). Especially, the  $\bullet O_2^-$  was almost depressed for the BiOCl during the photocatalytic-Fenton process (Fig. 7e).

Then, the variation of  $Fe^{2+}$  concentration in solution,  $H_2O_2$  conversion efficiency, and  $H_2O_2$  activation selectivity was also examined (Fig. 7f, Fig. S18-S19). For the BiOCl, the  $H_2O_2$  conversion efficiency was gradually increased when prolonging the irradiation time in the presence of a higher concentration of  $Fe^{2+}$  (Fig. S19a-S19b). But, the  $Fe^{2+}$  concentration decreased accordingly by prolonging the irradiation time through Fenton reaction ( $Fe^{2+} + H_2O_2 \rightarrow Fe^{3+} + \bullet OH + OH^-$ ). In terms of the core-shell BiOCl@Fe-BiOCl, the increasing  $H_2O_2$  conversion efficiency was higher than that of BiOCl. But, the concentration of Fe(II) for the BiOCl@Fe-BiOCl has retained at 0 mM and barely changed throughout the whole photocatalytic-Fenton process (Fig. S19c), implying that the Fe(II) still maintained in the shell layer and conducted Fe(III)/Fe(II) recycling well. The concentration of  $\bullet OH$  during the photocatalytic-Fenton process for BiOCl@Fe-BiOCl was ~28.9 times higher than that for BiOCl, and even ~2.05 times higher than that of BiOCl +  $Fe^{2+}$  (Fig. 7d). And the corresponding  $\bullet O_2^-$  concentration for BiOCl@Fe-BiOCl also was slightly higher than that of BiOCl (Fig. 7e). As compared with BiOCl +  $Fe^{2+}$  during the photocatalytic-Fenton process, the  $\bullet O_2^-$  concentration was much lower. Then, the selectivity of  $\bullet O_2^-$  and  $\bullet OH$  over different samples were examined [54]. In terms of the BiOCl, the percentage of  $\bullet O_2^-$  (57.80 %) was higher than  $\bullet OH$  (42.20 %), suggesting that  $\bullet O_2^-$  was predominant active species during the photocatalytic process. Comparatively, the  $\bullet O_2^-$  percentage was nearly depressed, and the  $\bullet OH$  selectivity gradually reached 91.13 % for the BiOCl +  $Fe^{2+}$  through the Fenton reaction (Fig. S19c). Whereas, the  $\bullet OH$  percentage also could reach 92.25 % for BiOCl@Fe-BiOCl, which was similar to that of BiOCl +  $Fe^{2+}$  during the photocatalytic-Fenton process ( $\equiv Fe(II) + H_2O_2 \rightarrow \equiv Fe(III) + \bullet OH + OH^-$ ), indicating its higher selective conversion of  $H_2O_2$  to  $\bullet OH$  through Fenton reaction (Fig. 7f).

The reactive sites including Bi, Bi-Fe, and Fe sites for the  $H_2O_2$  activation during the synergetic photocatalytic-Fenton process of core-shell BiOCl@Fe-BiOCl nanosheets were also investigated theoretically



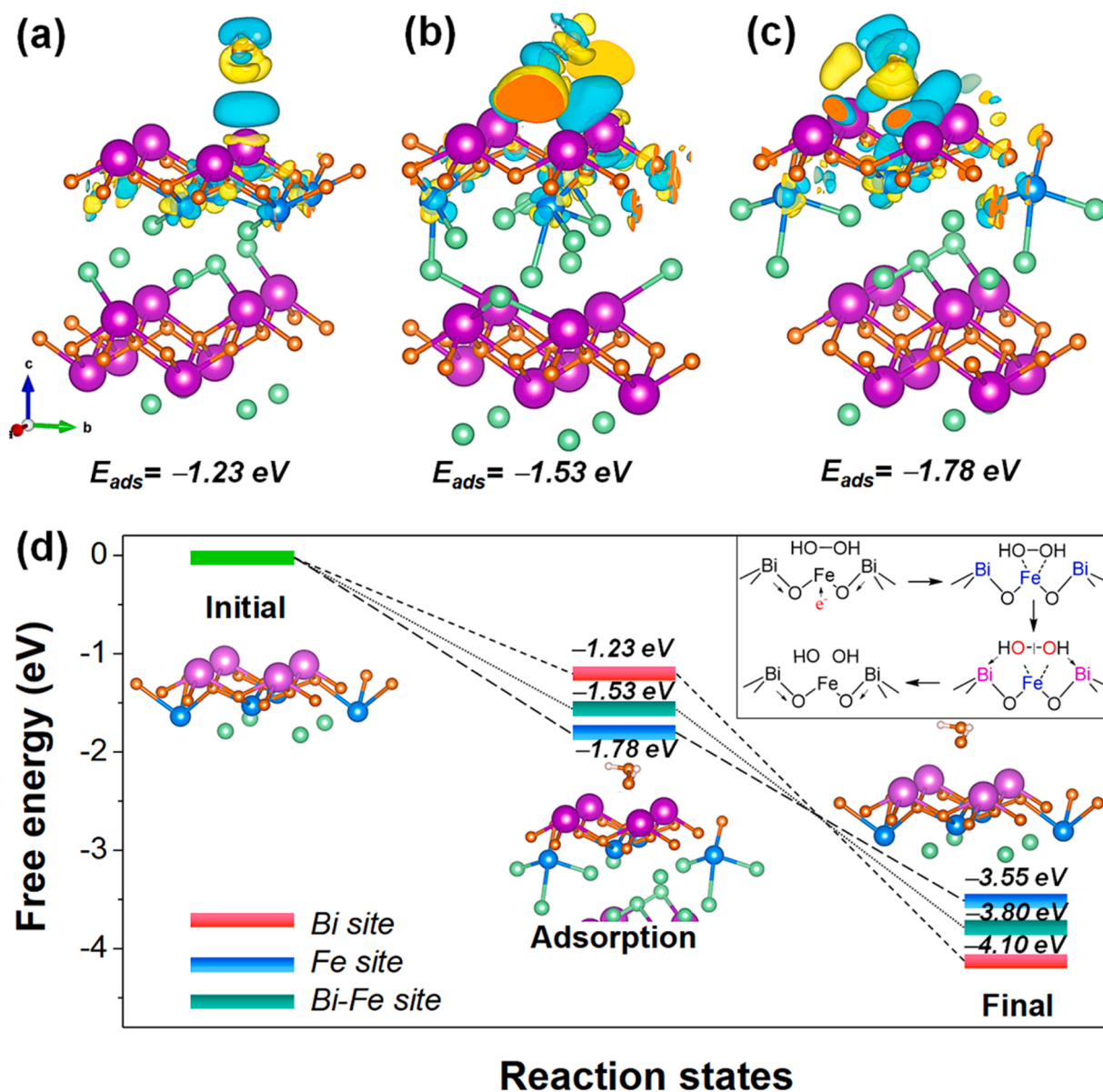


**Fig. 8.** The adsorption energy of  $\text{H}_2\text{O}_2$  on different sites and corresponding charge density differences of  $\text{BiOCl@Fe-BiOCl}$ , (a) Bi site, (b) Bi-Fe site, (c) Fe site (Yellow and blue iso-surfaces depict charge accumulation and charge depletion, respectively). (d) Calculated transition energy of  $\text{H}_2\text{O}_2$  activation to  $\bullet\text{OH}$  at different sites (inset with the plausible mechanism of  $\text{H}_2\text{O}_2$  activation).

through the DFT simulation (Fig. 8, Fig. S20). On the shell layer of  $\text{Fe-BiOCl}$ ,  $\text{H}_2\text{O}_2$  is bound to the Bi atom and Fe atom in a side-on bridging mode. However,  $\text{H}_2\text{O}_2$  is bound to the Bi-Fe atoms in a terminal end-on mode [55,56]. For the Bi atom site, the charges depleted on the Bi atom of  $\text{Fe-BiOCl}$  and accumulated on both O atoms of  $\text{H}_2\text{O}_2$ , and the structure of the  $\text{Fe-BiOCl}$  was barely changed (Fig. 8a). Similarly, the charges depleted on the Bi atom of  $\text{Fe-BiOCl}$  and accumulated on one O atom of  $\text{H}_2\text{O}_2$  when  $\text{H}_2\text{O}_2$  adsorbed on Bi-Fe sites. Notably, the structure of  $\text{Fe-BiOCl}$  was slightly distorted and the lengths of Fe-Cl bonds at the sub-layer of  $\text{Fe-BiOCl}$  were slightly decreased from  $\sim 2.75 \text{ \AA}$  to  $\sim 2.51 \text{ \AA}$  (Fig. 8b). Differently, the structure of  $\text{Fe-BiOCl}$  was further distorted that the lengths of Fe-Cl bonds were decreased to  $2.41 \text{ \AA}$  due to the substantial donation from Fe atoms when the  $\text{H}_2\text{O}_2$  adsorbed on the Fe atoms of  $\text{Fe-BiOCl}$ . Furthermore, the charges were more tended to deplete on the four Bi atoms and Fe atoms of near-surface, and accumulated on O atoms of  $\text{H}_2\text{O}_2$  (Fig. 8c). Then, the adsorption energy of  $\text{H}_2\text{O}_2$  on the Bi, Bi-Fe, and Fe sites of  $\text{Fe-BiOCl}$  were estimated to be  $-1.23 \text{ eV}$ ,  $-1.53 \text{ eV}$ , and  $-1.78 \text{ eV}$ , respectively. Obviously,  $\text{H}_2\text{O}_2$

was more inclined to adsorb on the Fe sites due to its lower adsorption energy. And the corresponding transition energies for reductive activation of  $\text{H}_2\text{O}_2$  into surface  $\bullet\text{OH}$  were  $-4.10 \text{ eV}$ ,  $-3.80 \text{ eV}$ , and  $-3.55 \text{ eV}$  (Fig. 8d). Apparently, the activation barrier of  $\text{H}_2\text{O}_2$  into surface  $\bullet\text{OH}$  at Fe atom site ( $-1.77 \text{ eV}$ ) was much lower than that at Bi ( $-2.87 \text{ eV}$ ) and Bi-Fe sites ( $-2.27 \text{ eV}$ ). These results indicated the Fe sites acted as active sites, which were more beneficial to activate  $\text{H}_2\text{O}_2$  into  $\bullet\text{OH}$ .

Furthermore, the plausible mechanism of the  $\text{H}_2\text{O}_2$  activation process was proposed based on the above charge density differences, transition energy, electron self-sufficient structure of  $\text{BiOCl@Fe-BiOCl}$ , and previous studies (Inset of Fig. 8d) [54,57,58]. Initially, the Bi atoms around a Fe atom with higher charge density donate the charge to the surrounding O atoms (Fig. 1g-h), increasing the charge accumulation on O atoms and remaining charge-depleted Bi atoms. Simultaneously, the electrons driven by the IEF of the  $\text{BiOCl}$  core were captured by the doped Fe(III), transiting Fe(III) state to Fe(II). Then, the  $\text{H}_2\text{O}_2$  adsorbed on the transited Fe(II) easily in a side-on bridging mode, increasing the

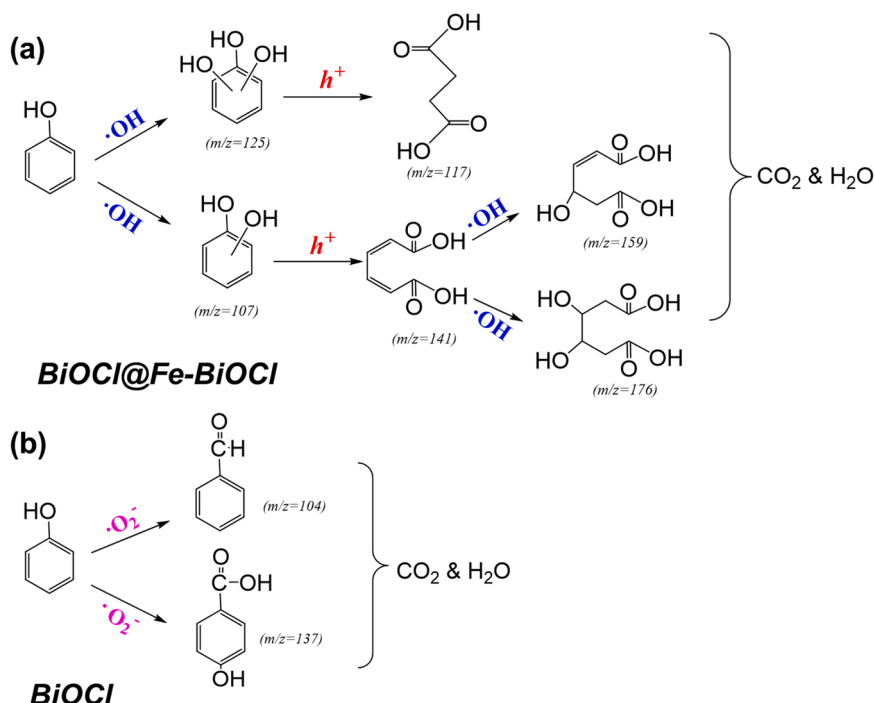


Fig. 9. Photocatalytic-Fenton mechanism of phenol degradation over (a) BiOCl@Fe-BiOCl, and (b) BiOCl.

charge density of the O–O bond of  $\text{H}_2\text{O}_2$ . Such O–O bond donated charges to the neighbor depleted Bi atoms and activated  $\text{H}_2\text{O}_2$  into  $\bullet\text{OH}$ . And the  $\bullet\text{OH}$  can be dissociated from the Fe atom site easily due to the lower barrier, further participating in the degradation process of phenol. Meanwhile, the Fe(II) transitioned back into the Fe(III) state in the structure.

Based on the above-mentioned results,  $\text{H}_2\text{O}_2$  could be activated into  $\bullet\text{OH}$  efficiently at Fe sites of Fe-BiOCl sheets via Fenton reaction, and the surface enriched  $h^+$  through photocatalysis are synergetic roles to react with phenol. The phenol degradation pathways over core-shell BiOCl@Fe-BiOCl nanosheets and BiOCl nanosheets were proposed by employing the LC-MS to analyze the intermediates during the photocatalytic process (Fig. 9, Fig. S21-S22). In the presence of core-shell BiOCl@Fe-BiOCl nanosheets, the efficient converted  $\bullet\text{OH}$  as primary radicals attack the benzene rings to produce benzene- $\text{OH}$  adducts [59], as presented in Fig. 9a. Then, these adducts were gradually transitioned into different carboxylic acids with the assistance of  $h^+$  for benzene ring-open, and then mineralized completely. The synergetic effect of  $\bullet\text{OH}$  and  $h^+$  promote the degradation and mineralization of phenol during this synergetic photocatalytic-Fenton process [60]. Comparatively, the hydroxyl group of phenol over BiOCl was oxidized into aldehyde and carboxylic acid through the oxidation of  $\bullet\text{O}_2^-$  predominately. The benzene rings of these benzaldehyde and benzoic acids were unable to be cleaved by the  $\bullet\text{O}_2^-$  efficiently, resulting in the lower mineralization of phenol over BiOCl (Fig. 9b).

#### 4. Conclusions

In this work, electron self-sufficient core-shell BiOCl@Fe-BiOCl nanosheets were prepared to boost the degradation and mineralization of phenol through synergetic photocatalytic-Fenton. This electron self-sufficient structure was established by engaging the IEF of the BiOCl core and electron-capture centers of doped Fe from the Fe-BiOCl shell, which was of benefit to the spatial charge separation during the photocatalytic process. Simultaneously, the Fe(III)/Fe(II) recycling and surface-enriched  $h^+$  also can be achieved in these core-shell BiOCl@Fe-BiOCl nanosheets through the Fenton reaction. The surface enriched  $h^+$  of BiOCl@Fe-BiOCl catalysts and accumulated  $\bullet\text{OH}$  through the Fenton

reaction played a synergetic effect on superior degradation and mineralization performances of phenol. The reaction constant rate of BiOCl@Fe-BiOCl nanosheets under full spectra ( $0.03843 \text{ min}^{-1}$ ) and visible light irradiation ( $0.0284 \text{ min}^{-1}$ ) were  $\sim 42$  and  $95$  times higher than that of pristine BiOCl. Furthermore,  $\sim 64\%$  mineralization of phenol over BiOCl@Fe-BiOCl was achieved within 60 min, which was 3.40 times over that of BiOCl in the presence of  $\text{H}_2\text{O}_2$ . This work provides the rational design of a sophisticated structure of catalysts for spatial charge separation, enhanced Fe(III)/Fe(II) recycling, boosted catalytic activity and mineralization ability of phenol.

#### CRediT authorship contribution statement

**Zhaohui Wu:** Design, Validation, Methodology, Data analysis, Writing - original draft, Writing - review & editing. **Jie Shen:** Visualization, Investigation. **Wenlu Li:** Visualization, Investigation. **Junshan Li:** Review. **Donghao Xia:** Visualization, Investigation. **Difa Xu:** Review. **Shiying Zhang:** Supervision, Review, Funding acquisition. **Yongfa Zhu:** Overall supervision, Resources, Writing - review & editing.

#### Declaration of Competing Interest

The authors declare that they have no known competing financial interests or personal relationships that could have appeared to influence the work reported in this paper.

#### Data Availability

No data was used for the research described in the article.

#### Acknowledgements

This work was supported by the Natural Science Foundation of Hunan Province (2019JJ50686), Scientific Research Fund of Hunan Provincial Education Department (20B055), NSFC (52174238, 22136002), Changsha University, and Tsinghua University.

## Appendix A. Supporting information

Supplementary data associated with this article can be found in the online version at [doi:10.1016/j.apcatb.2023.122642](https://doi.org/10.1016/j.apcatb.2023.122642).

## References

- [1] E.M. Siedlecka, Application of bismuth-based photocatalysts in environmental protection, in: Inamuddin, A.M. Asiri, E. Lichtfouse (Eds.), *Nanophotocatalysis and Environmental Applications*, Environmental Chemistry for a Sustainable World, Springer, Cham, 2019, pp. 87–118.
- [2] S. Taghipour, S.M. Hosseini, B. Ataie-Ashtiani, Engineering nanomaterials for water and wastewater treatment: Review of classifications, properties and applications, *N. J. Chem.* 43 (2019) 7902–7927.
- [3] H.Q. Lu, J.F. Yao, Recent advances in liquid-phase heterogeneous photocatalysis for organic synthesis by selective oxidation, *Curr. Org. Chem.* 18 (2014) 1365–1372.
- [4] D.D. Cui, L. Wang, Y. Du, W.C. Hao, J. Chen, Photocatalytic reduction on bismuth-based p-block semiconductors, *ACS Sustain. Chem. Eng.* 6 (2018) 15936–15953.
- [5] J. Fujisawa, A. Osawa, M. Hanaya, A strategy to minimize the energy offset in carrier injection from excited dyes to inorganic semiconductors for efficient dye-sensitized solar energy conversion, *Phys. Chem. Chem. Phys.* 18 (2016) 22244–22253.
- [6] X.L. Jin, L.Q. Ye, H.Q. Xie, G. Chen, Bismuth-rich bismuth oxyhalides for environmental and energy photocatalysis, *Coord. Chem. Rev.* 349 (2017) 84–101.
- [7] S. Weng, Z. Pei, Z. Zheng, J. Hu, P. Liu, Exciton-free, nonsensitized degradation of 2-naphthol by facet-dependent BiOCl under visible light: novel evidence of surface-state photocatalysis, *ACS Appl. Mater. Inter.* 5 (2013) 12380–12386.
- [8] J. Jiang, K. Zhao, X. Xiao, L. Zhang, Synthesis and facet-dependent photoreactivity of BiOCl single-crystalline nanosheets, *J. Am. Chem. Soc.* 134 (2012) 4473–4476.
- [9] C.Y. Wang, Y.J. Zhang, W.K. Wang, D.N. Pei, G.X. Huang, J.J. Chen, X. Zhang, H. Q. Yu, Enhanced photocatalytic degradation of bisphenol A by Co-doped BiOCl nanosheets under visible light irradiation, *Appl. Catal. B-Environ.* 221 (2018) 320–328.
- [10] J.G. Sun, S.J. Wu, S.Z. Yang, Q. Li, J.W. Xiong, Z.Z. Yang, L. Gu, X.X. Zhang, L. D. Sun, Enhanced photocatalytic activity induced by  $sp^3$  to  $sp^2$  transition of carbon dopants in BiOCl crystals, *Appl. Catal. B-Environ.* 221 (2018) 467–472.
- [11] Y. Tang, F. Teng, Y.D. Kan, L.M. Yang, Z.L. Liu, W.H. Gu, A. Zhang, W.Y. Hao, Y. R. Teng, Investigation of the charges separation and transfer behavior of BiOCl/BiF<sub>3</sub> heterojunction, *Appl. Catal. B-Environ.* 205 (2017) 412–420.
- [12] L.M. Sun, L. Xiang, X. Zhao, C.J. Jia, J. Yang, Z. Jin, X.F. Cheng, W.L. Fan, Enhanced visible-light photocatalytic activity of BiO/BiOCl heterojunctions: Key role of crystal facet combination, *ACS Catal.* 5 (2015) 3540–3551.
- [13] Y. Mi, L.Y. Wen, Z.J. Wang, D.W. Cao, R. Xu, Y.G. Fang, Y.L. Zhou, Y. Lei, Fe(III) modified BiOCl ultrathin nanosheet towards high-efficient visible-light photocatalyst, *Nano Energy* 30 (2016) 109–117.
- [14] H. Li, L.Z. Zhang, Oxygen vacancy induced selective silver deposition on the {001} facets of BiOCl single-crystalline nanosheets for enhanced Cr(VI) and sodium pentachlorophenate removal under visible light, *Nanoscale* 6 (2014) 7805–7810.
- [15] X. Zhang, X.B. Wang, L.W. Wang, W.K. Wang, L.L. Long, W.W. Li, H.Q. Yu, Synthesis of a highly efficient BiOCl single-crystal nanodisk photocatalyst with exposing {001} facets, *ACS Appl. Mater. Inter.* 6 (2014) 7766–7772.
- [16] H. Zhao, X. Liu, Y.M. Dong, Y.M. Xia, H.J. Wang, X.M. Zhu, Fabrication of a Z-Scheme {001}/{110} facet heterojunction in BiOCl to promote spatial charge separation, *ACS Appl. Mater. Inter.* 12 (2020) 31532–31541.
- [17] L. Zhang, W.Z. Wang, S.M. Sun, D. Jiang, E.P. Gao, Selective transport of electron and hole among {001} and {110} facets of BiOCl for pure water splitting, *Appl. Catal. B-Environ.* 162 (2015) 470–474.
- [18] H. Li, F. Qin, Z.P. Yang, X.M. Cui, J.F. Wang, L.Z. Zhang, New reaction pathway induced by plasmon for selective Benzyl alcohol oxidation on BiOCl possessing oxygen vacancies, *J. Am. Chem. Soc.* 139 (2017) 3513–3521.
- [19] K. Zhao, L.Z. Zhang, J.J. Wang, Q.X. Li, W.W. He, J.J. Yin, Surface structure-dependent molecular oxygen activation of BiOCl single-crystalline nanosheets, *J. Am. Chem. Soc.* 135 (2013) 15750–15753.
- [20] L. Wang, D.D. Lv, F. Dong, X.L. Wu, N.Y. Cheng, J. Scott, X. Xu, W.C. Hao, Y. Du, Boosting visible-light-driven photo-oxidation of BiOCl by promoted charge separation via vacancy engineering, *ACS Sustain. Chem. Eng.* 7 (2019) 3010–3017.
- [21] H. Li, J. Shang, H.J. Zhu, Z.P. Yang, Z.H. Ai, L.Z. Zhang, Oxygen vacancy structure associated photocatalytic water oxidation of BiOCl, *ACS Catal.* 6 (2016) 8276–8285.
- [22] M. Sun, C.H. Chu, F.L. Geng, X.L. Lu, J.H. Qu, J. Crittenden, M. Elimelech, J. H. Kim, Reinventing Fenton chemistry: Iron oxychloride nanosheet for pH-insensitive H<sub>2</sub>O<sub>2</sub> activation, *Environ. Sci. Tech. Lett.* 5 (2018) 186–191.
- [23] A.V. Vorontsov, Advancing Fenton and photo-Fenton water treatment through the catalyst design, *J. Hazard. Mater.* 372 (2019) 103–112.
- [24] M. Gao, D. Zhang, X. Pu, H. Li, W. Li, X. Shao, D. Lv, B. Zhang, J. Dou, Combustion synthesis of Fe-doped BiOCl with high visible-light photocatalytic activities, *Sep. Purif. Technol.* 162 (2016) 114–119.
- [25] K.-X. Xin Zhong, Di Wu, Xia-Yu Ye, Wei Huang, Bin-Xue Zhou, Enhanced photocatalytic degradation of levofloxacin by Fe-doped BiOCl nanosheets under LED light irradiation, *Chem. Eng. J.* 383 (2020), 123148.
- [26] X.L. Haoyuan Wu, Hua Xu, Xinmin Yang, Jinhua Ye, Efficient photodegradation of 2-chloro-4-nitrophenol over Fe-doped BiOCl nanosheets with oxygen vacancy, *Catal. Sci. Technol.* 11 (2021) 5119–5124.
- [27] K.M. Arjunan Babuponnusami, A review on Fenton and improvements to the Fenton process for wastewater treatment, *J. Environ. Chem. Eng.* 2 (2014) 557–572.
- [28] X. Zhang, J. Wang, B. Xiao, Y. Pu, Y. Yang, J. Geng, D. Wang, X. Chen, Y. Wei, K. Xiong, Y. Zhu, Resin-based photo-self-Fenton system with intensive mineralization by the synergistic effect of holes and hydroxyl radicals, *Appl. Catal. B-Environ.* 315 (2022), 121525.
- [29] Z.H. Wu, J. Shen, N. Ma, Z.F. Li, M. Wu, D.F. Xu, S.Y. Zhang, W.H. Feng, Y.F. Zhu, Bi<sub>4</sub>O<sub>5</sub>Br<sub>2</sub> nanosheets with vertical aligned facets for efficient visible-light-driven photodegradation of BPA, *Appl. Catal. B-Environ.* 286 (2021), 119937.
- [30] J.F.G. Kresse, Efficiency of ab-initio total energy calculations for metals and semiconductors using a plane-wave basis set, *Comp. Mater. Sci.* 6 (1996) 15–50.
- [31] P.E. Blöchl, Projector augmented-wave method, *Phys. Rev. B* 50 (1994) 17953.
- [32] John P. Perdew, J.A. Chevary, S.H. Vosko, Koblar A. Jackson, Mark R. Pederson, D. J. Singh, Carlos Fiolhais, Atoms, molecules, solids, and surfaces: Applications of the generalized gradient approximation for exchange and correlation, *Phys. Rev. B* 46 (1993) 6671.
- [33] G. Kresse, D. Joubert, From ultrasoft pseudopotentials to the projector augmented-wave method, *Phys. Rev. B* 59 (1999) 1758–1775.
- [34] J.P. Perdew, K. Burke, M. Ernzerhof, Generalized gradient approximation made simple, *Phys. Rev. Lett.* 77 (1996) 3865–3868.
- [35] A.J. Grimme S, S. Ehrlich, H. Krieg, A consistent and accurate ab initio parametrization of density functional dispersion correction (DFT-D) for the 94 elements H-Pu, *J. Chem. Phys.* 132 (2010), 154104.
- [36] H.B. Yu, D. Ge, Y. Wang, S.Y. Zhu, X.H. Wang, M.X. Huo, Y. Lu, Facile synthesis of Bi-modified Nb-doped oxygen defective BiOCl microflowers with enhanced visible-light-driven photocatalytic performance, *J. Alloy Compd.* 786 (2019) 155–162.
- [37] L. Wang, D.D. Lv, Z.J. Yue, H. Zhu, L. Wang, D.F. Wang, X. Xu, W.C. Hao, S.X. Dou, Y. Du, Promoting photoreduction properties via synergetic utilization between plasmonic effect and highly active facet of BiOCl, *Nano Energy* 57 (2019) 398–404.
- [38] M. Li, Y.H. Zhang, X.W. Li, Y.G. Wang, F. Dong, L.Q. Ye, S.X. Yu, H.W. Huang, Nature-derived approach to oxygen and chlorine dual-vacancies for efficient photocatalysis and photoelectrochemistry, *ACS Sustain. Chem. Eng.* 6 (2018) 2395–2406.
- [39] J. Zhang, M.X. Yang, Y. Lian, M.L. Zhong, J.Q. Sha, G.D. Liu, X.F. Zhao, S.J. Liu, Ce<sup>3+</sup> self-doped CeOx/FeOCl: an efficient Fenton catalyst for phenol degradation under mild conditions, *Dalton T.* 48 (2019) 3476–3485.
- [40] G.L. Jian Zhang, Shaojie Liu, 2D/2D FeOCl/graphite oxide heterojunction with enhanced catalytic performance as a photo-Fenton catalyst, *N. J. Chem.* 42 (2018) 6896–6902.
- [41] Z.W. Zou, H.M. Xu, D.Y. Li, J.Y. Sun, D.S. Xia, Facile preparation and photocatalytic activity of oxygen vacancy rich BiOCl with {001} exposed reactive facets, *Appl. Surf. Sci.* 463 (2019) 1011–1018.
- [42] H. Li, L.Z. Zhang, Photocatalytic performance of different exposed crystal facets of BiOCl, *J. Curr. Opin. Green. Sust.* 6 (2017) 48–56.
- [43] Z. Wu, J. Jing, K. Zhang, W. Li, J. Yang, J. Shen, S. Zhang, K. Xu, S. Zhang, Y. Zhu, Epitaxial BiP<sub>5</sub>O<sub>14</sub> layer on BiO nanosheets enhancing the photocatalytic degradation of phenol via interfacial internal-electric-field, *Appl. Catal. B-Environ.* 307 (2022), 121153.
- [44] J. Li, H. Li, G.M. Zhan, L.Z. Zhang, Solar water splitting and nitrogen fixation with layered bismuth oxyhalides, *Acc. Chem. Res.* 50 (2017) 112–121.
- [45] M. Li, H.W. Huang, S.X. Yu, N. Tian, Y.H. Zhang, Facet, junction and electric field engineering of bismuth-based materials for photocatalysis, *ChemCatChem* 10 (2018) 4477–4496.
- [46] J. Jing, J. Yang, Z. Zhang, Y. Zhu, Supramolecular zinc porphyrin photocatalyst with strong reduction ability and robust built-in electric field for highly efficient hydrogen production, *Adv. Energy Mater.* 11 (2021), 2101392.
- [47] Z. Zhang, X. Chen, H. Zhang, W. Liu, W. Zhu, Y. Zhu, A highly crystalline perylene imide polymer with the robust built-in electric field for efficient photocatalytic water oxidation, *Adv. Mater.* 32 (2020), 1907746.
- [48] Y. Guo, W. Shi, Y. Zhu, Internal electric field engineering for steering photogenerated charge separation and enhancing photoactivity, *EcoMat* 1 (2019), e12007.
- [49] M. Li, S.X. Yu, H.W. Huang, X.W. Li, Y.B. Feng, C. Wang, Y.G. Wang, T.Y. Ma, L. Guo, Y.H. Zhang, Unprecedented eighteen-faceted BiOCl with a ternary facet junction boosting cascade charge flow and photo-redox, *Angew. Chem. Int. Ed.* 58 (2019) 9517–9521.
- [50] J. Jing, J. Yang, W. Li, Z. Wu, Y. Zhu, Construction of interfacial electric field via dual-porphyrin heterostructure boosting photocatalytic hydrogen evolution, *Adv. Mater.* 34 (2022), 2106807.
- [51] Y. Chen, F. Wang, Y.H. Cao, F.Y. Zhang, Y.Z. Zou, Z.A. Huang, L.Q. Ye, Y. Zhou, Interfacial oxygen vacancy engineered two-dimensional g-C<sub>3</sub>N<sub>4</sub>/BiOCl heterostructures with boosted photocatalytic conversion of CO<sub>2</sub>, *ACS Appl. Energy Mater.* 3 (2020) 4610–4618.
- [52] J.X. Low, J.G. Yu, M. Jaroniec, S. Wageh, A.A. Al-Ghamdi, Heterojunction photocatalysts, *Adv. Mater.* 29 (2017), 1601694.
- [53] F. Tian, G.F. Li, H.P. Zhao, F.X. Chen, M. Li, Y.L. Liu, R. Chen, Residual Fe enhances the activity of BiOCl hierarchical nanostructure for hydrogen peroxide activation, *J. Catal.* 370 (2019) 265–273.
- [54] C. Ling, X. Liu, H. Li, X. Wang, H. Gu, K. Wei, M. Li, Y. Shi, H. Ben, G. Zhan, C. Liang, W. Shen, Y. Li, J. Zhao, L. Zhang, Atomic-layered Cu<sub>5</sub> nanoclusters on FeS<sub>2</sub> with dual catalytic sites for efficient and selective H<sub>2</sub>O<sub>2</sub> activation, *Angew. Chem. Int. Ed.* 61 (2022), e202200670.
- [55] H. Li, H. Shang, X.M. Cao, Z.P. Yang, Z.H. Ai, L. Zhang, Oxygen vacancies mediated complete visible light NO oxidation via side-on bridging superoxide radicals, *Environ. Sci. Technol.* 52 (2018) 8659–8665.



- [56] H. Li, J. Shang, J.G. Shi, K. Zhao, L.Z. Zhang, Facet-dependent solar ammonia synthesis of BiOCl nanosheets via a proton-assisted electron transfer pathway, *Nanoscale* 8 (2016) 1986–1993.
- [57] C. Chen, Y. Wang, Y. Huang, J. Hua, W. Qu, D. Xia, C. He, V.K. Sharma, D. Shu, Overlooked self-catalytic mechanism in phenolic moiety-mediated Fenton-like system: Formation of Fe(III) hydroperoxide complex and co-treatment of refractory pollutants, *Appl. Catal. B-Environ.* 321 (2023), 122062.
- [58] G.L. Puma, A. Brucato, Dimensionless analysis of slurry photocatalytic reactors using two-flux and six-flux radiation absorption–scattering models, *Catal. Today* 122 (2007) 78–90.
- [59] J.J. An, L.H. Zhu, N. Wang, Z. Song, Z.Y. Yang, D.Y. Du, H.Q. Tang, Photo-Fenton like degradation of tetrabromobisphenol A with graphene-BiFeO<sub>3</sub> composite as a catalyst, *Chem. Eng. J.* 219 (2013) 225–237.
- [60] Y. Ding, P. Zhou, H. Tang, Visible-light photocatalytic degradation of bisphenol A on NaBiO<sub>3</sub> nanosheets in a wide pH range: A synergistic effect between photocatalytic oxidation and chemical oxidation, *Chem. Eng. J.* 291 (2016) 149–160.